Astron. Astrophys. 354, 453–466 (2000)

ASTRONOMY AND ASTROPHYSICS

Dust in PG quasars as seen by ISO⋆

M. Haas[1], S.A.H. Müller[1,2], R. Chini[2], K. Meisenheimer[1], U. Klaas[1], D. Lemke[1], E. Kreysa[3], and M. Camenzind[4]

[1] Max-Planck-Institut für Astronomie (MPIA), Königstuhl 17, 69117 Heidelberg, Germany
[2] Astronomisches Institut, Universität Bochum, 44780 Bochum, Germany
[3] Max-Planck-Institut für Radioastronomie, Auf dem Hügel 69, 53121 Bonn, Germany
[4] Landessternwarte Heidelberg, Königstuhl, 69117 Heidelberg, Germany

Received 18 August 1999 / Accepted 9 December 1999

Abstract. Infrared to millimeter spectral energy distributions (SEDs) have been obtained for a random sample of 17 Palomar Green quasars. The observations were carried out between 4.8 and 200 μm with ISO and supplemented for ten sources with IRAM at 1.3 mm. Eight sources were detected in the far infrared for the first time. The SEDs provide evidence for considerable dust emission and do not support the existence of dust-free, naked quasars. The SEDs resemble those of warm ultraluminous infrared galaxies (ULIRGs). The SEDs show a variety of shapes (power-law, mid-infrared dominated, and far-infrared dominated), suggesting the influence of different heating mechanisms. The mid- and far-infrared luminosities are correlated, suggesting a dependence between the heating mechanisms. The role of AGNs and starbursts for the dust heating is discussed, as well as the link between general ULIRGs and dust-enshrouded quasars.

Key words: galaxies: fundamental parameters – galaxies: photometry – galaxies: quasars: general – infrared: galaxies

1. Introduction

The Palomar-Green catalog (Schmidt & Green 1983) provides a well defined optically selected sample of 114 quasars for some of which the first statistically useful mid- and far-infrared detections were obtained by IRAS (cf. Neugebauer et al. 1986, Sanders et al. 1989). The current understanding of the ultraviolet to far-infrared continua of PG quasars is guided by a three component model (Barvainis 1990; Rowan-Robinson 1995) consisting of

1) a UV-optical component due to the black hole accretion disk,
2) a central 'AGN' dust component spatially associated with the narrow line region, showing up in the NIR-MIR at $3 - 25\,\mu$m with the UV-optical photons as primary heating source,
3) a 'starburst' (SB) dust component represented by the FIR $60 - 100\,\mu$m emission, probably radiating from extended regions in the host galaxy.

The observational basis in the IR is still limited. Only a moderate fraction of the 114 optically bright PG quasars were detected by IRAS in the representative MIR 25 μm and FIR 60 μm bands: 36 radio-quiet sources used by Barvainis (1990) and only 24 sources using stricter selection criteria by Rowan-Robinson (1995).

An issue of debate is the relation between AGN and starburst components: On the one hand a wide variety of shapes in the IR continua was reported as favoring independent components (Barvainis 1990); on the other hand a correlation between the luminosity of these two components was found (Rowan-Robinson 1995).

A second topic of the current research is the evolutionary link between ultraluminous infrared galaxies (ULIRGs) and quasars: among the bright ULIRGs, all those (12 out of 12 sources) with 'warm' MIR to FIR colors ($F_{25\mu m}/F_{60\mu m} > 0.2$) exhibit Seyfert type spectra, i.e. signatures of quasars (Sanders et al. 1988b). Although not every ULIRG needs to evolve into a quasar, every quasar appears to be inevitably accompanied by a starburst (Rowan-Robinson 1995). This last statement, however, is based on considering only quasars detected in the FIR and we emphasize that there could be 'dusty' as well as 'naked' quasars – the latter group possibly being more evolved. The evolutionary link between ULIRGs and quasars and the detection of naked quasars requires the study of an optically selected sample and observations at high sensitivity.

2. The sample

Within the *ISO European Central Quasar Programme* we have observed different samples of quasars, and the first results on a few bright sources including three PG quasars have already been published (Haas et al. 1998a). Here we report on our full sample of 17 PG quasars. Originally all PG quasars were selected having B<16 mag and lying in the sky area visible by the ISO satellite. About one third of the PG sample was contained in the *ISO European Central Quasar Programme*, the rest was covered by the *US ISO Quasar Key Project* (Wilkes et al. 1999; Hooper et al. 1999). During the actual execution of the first

Send offprint requests to: Martin Haas (haas@mpia-hd.mpg.de)

⋆ Based on observations with the Infrared Space Observatory ISO, an ESA project with instruments funded by ESA Member States (especially the PI countries: France, Germany, the Netherlands and the United Kingdom) and with the participation of ISAS and NASA.

measurements it turned out that the occurrence of high energy particle glitches and the presence of cirrus structure required a more time consuming measurement mode. Therefore the samples had to be reduced due to (1) time constraints, (2) sources with low cirrus foreground for optimum detectability and (3) further sky visibility constraints. From the originally selected sample, 17 sources were observed. Three of our sources are also contained in the sample of 24 PG quasars by Rowan-Robinson (1995). Though not statistically complete, our data represent a fair random sample with a well balanced coverage of redshift range from nearby ($z \approx 0$) to distant ($z = 2$) objects.

3. Observations and data reduction

3.1. ISO data

The observations were performed with ISOPHOT (Lemke et al. 1996), the photometer on board ISO (Kessler et al. 1996). The observing modes (Klaas et al. 1994) comprise low sensitivity chopped measurements and, adopted in the course of the ISO mission, high sensitivity small maps. The on-source integration time was chosen between 16 and 360 s, depending on the source and cirrus brightness, and the detector and filter combination. The apertures used in flux derivation are 23″ circular for 4.8-25μm (P1, P2 detectors), and 46″ square for 60-100μm (i.e. only the central pixel of the 3×3 pixels C100 array is used). For 150-200μm they are 92″ square in case of maps (where the source is centered on a pixel) and 184″ square in the case of chopped observations (where the source is centered in the mid of the 2×2 pixels C200 array).

The data were reduced using the ISOPHOT Interactive Analysis tool (PIA[1] V7.2.2e), together with the calibration data set V4.0 (Laureijs et al. 1998). This included correction for the electronics' non-linearity, deglitching (removal of data sections disturbed by cosmic particle events), correction for signal dependence on the reset interval time, and correction for signal loss with chopper offset. The calibration of detector responsivity and its changes was performed using associated measurements of the thermal fine calibration source on board. Finally, the source fluxes were corrected for the aperture size assuming an unresolved point source and, in the case of chopped measurements, for transient effects. The accuracy of the absolute photometric calibration depends mainly on systematic errors as described in Laureijs & Klaas (1999), and it is currently known to be better than 30% (Klaas & Radovich 1998; Klaas et al. 1998b).

For the NIR/MIR observations a 23″ aperture in combination with the P1 and P2 detectors was used. This is smaller than the standard calibrated apertures (52″ and 79″, resp.) for these wavelength ranges, but it was chosen in order to improve the contrast against "sky background". As a calibration check for this small aperture we analysed the SED shape of the background positions. These SEDs should be smooth and consistent with a model of two λ^{-2} modified Planckian components – one at T = 265 K for the zodiacal light, one at T = 20 K for the galactic cirrus – and the absolute background brightnesses should on average be comparable with DIRBE/COBE results. For the 23″ aperture we corrected for systematic features we found compared with the model fits (peaks of plus 40% for the 12.8 μm filter and dips of minus 40 % for the 20 and 25 μm filters).

The results obtained with the algorithms provided in PIA often showed relatively large errors due to random outliers. These prevented a formal 3-sigma detection, though the visual inspection of, for example, a chopped signal series left no doubt in the source detection. Statistically a sigma-clipping could help to remove the outliers, but a general "blind" application of sigma-clipping sometimes results in unrealistically small errors – recognisable in particular in case of a non-detection, e.g. when a 3-sigma upper limit at 60 μm lies far below a clear detection at 25 and 100 μm. Also, for the raster maps the creation of the maps from a superposition of the time series of different detector pixels introduced noise due to drift and flatfield differences between the detector pixels, which prevented optimal source detections. Therefore we developed advanced reduction techniques which are described in detail in the Appendix. For straight forward reading, briefly, the methods are:

(1) For the chopped measurements we applied a Fourier analysis. In Fourier space the source signal shows up at the chopper frequency, while the noise of the chopped sequence forms some kind of baseline distributed over all frequencies. This technique is quite robust against single outlier chopper plateau signals and the effect of long term detector drift. Its main advantage is a consistent noise estimate which also accounts for the number of chopper plateaux.

(2) For the small raster maps we did not extract the source flux from the final maps. Instead, we analysed the signal time series while each detector pixel crossed the source. This technique allows immediate recognition of bad or outlying signals. Furthermore, a long term detector drift could increase the scatter in the background values of a map, while for the time series of each detector pixel the background can be estimated more accurately from the raster positions located immediately before and after the source was hit.

(3) For several marginal detections at two wavelengths, e.g. at 60 and 100 μm, we co-added the raster maps irrespective of the different wavelengths. In one case (PG 0044+030) two 2-sigma non-detections could then be improved to a 3-sigma detection – with an average wavelength of 80 μm adopted. The reliability of the very faint 80 μm detection (shown in Fig. A3, Appendix) is supported also by the independent detection at 170 μm.

Since the cirrus noise can be quite high (cf. Herbstmeier et al. 1998), we have also checked for it in the C100 and C200 array data, i.e. the wavelength range in which the galactic cirrus structures may lead to artificial source detections. However, our observation strategy was optimised to measure a source which has a *known* position. (This task is different from creating a big map and identifying peaks therein with sources.) Thus in our measurements the conditions (i.e. signal/noise ratio) for these

[1] PIA is a joint development by the ESA Astrophysics Division and the ISOPHOT consortium led by the MPI für Astronomie, Heidelberg. Contributing institutes are DIAS, RAL, AIP, MPIK, and MPIA.

known source positions were better than for any other sky position. Nevertheless, we accepted as detections only those cases where the source was clearly visible above the cirrus noise. Furthermore, if our derived (faint) source fluxes were dominated by cirrus noise contributions, we would expect spectral energy distributions with a 17-20 K dust temperature similar to that of the galactic cirrus. But this is not the case – the dust temperatures of our quasars are much higher.

3.2. IRAM data

The 1.3 mm continuum observations were carried out with the MPIfR 19 channel bolometer array (Kreysa et al. 1998). The array was mounted at the Nasmyth focus in a fixed orientation. The chopping secondary mirror of the telescope was used to modulate the beams at 2 Hz in Azimuth direction with an amplitude of 32″. In the so called ON-OFF-OFF-ON observing mode, beams were switched after each 10 s of integration time. While the source signal was detected in the central channel only, the residual fluctuation of sky emission (sky-noise) was monitored in the neighboring channels with the purpose of cancelling this noise for the signal channel. Depending on the source strength, a sufficient number of ON-OFF-OFF-ONs was accumulated and the final source signal obtained as a weighted average. The atmospheric transmission was determined by measurement series at various zenith distances (skydips); the calibration was established by observations of Uranus. The absolute uncertainty of the 1.3 mm fluxes is estimated to be around 25%.

4. Results

The IR and mm fluxes are listed in Table 1. The four brightest sources detected by IRAS were also well detected by ISO, and the fluxes all agree within 15%. Two sources marginally detected by IRAS are now clearly confirmed by ISO. In addition, eight new detections in the IR could be achieved. For the remaining three out of 17 sources, upper limits are provided at all wavelengths. Fig. 1 illustrates that the cirrus background brightness mainly determines whether detections or upper limits can be achieved, and that the upper limits are not biased at high redshift. Ten sources were measured at 1.3 mm; four sources were detected and good upper limits were provided for the remaining six sources.

The spectral energy distributions (SEDs, as measured, not corrected for redshift) are shown in Fig. 2 supplemented by data from the literature. Note that the temperature values of the blackbodies shown in Fig. 2 are corrected for redshift. The most remarkable feature of the SEDs is the steady flux increase from the NIR over the MIR peaking in the FIR regime at about 60 μm (PG 1411+442 peaks already at 25 μm), followed by the begin of the Rayleigh-Jeans tail which steeply falls off towards the 1.3 mm data points (except for the radio loud object PG 1302-102, see below). This is most obvious for PG 1613+658 (and PG 1634+706) with a spectral index $\alpha_{200-1300\mu m} \approx 3.1$ (> 2.6). It again demonstrates that the radiation is not due to synchrotron emission but rather originates

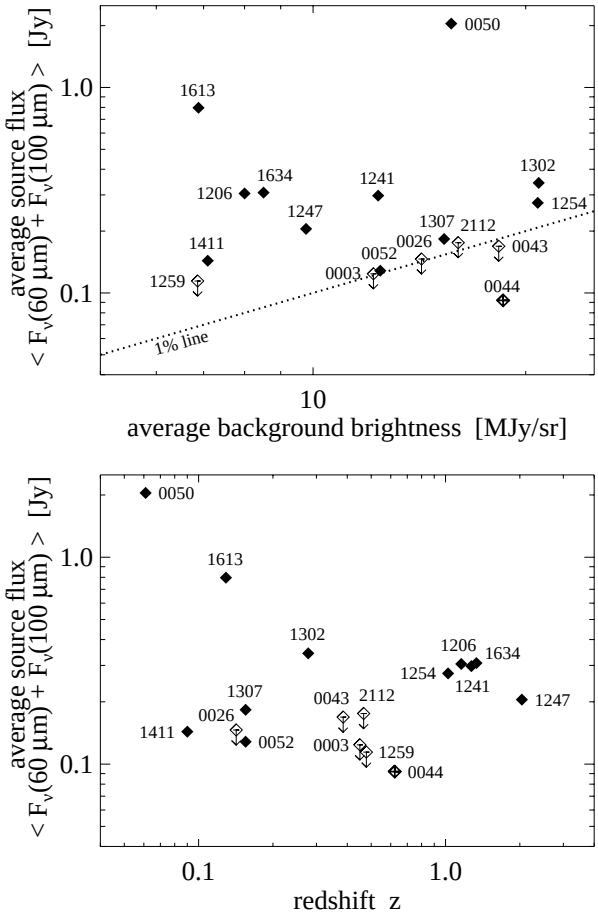

Fig. 1. Source flux versus background brightness *(top)* and redshift *(bottom)*, respectively. The source flux and background brightness were averaged from the 60 and 100 μm data, similarly as for the last column in Table 1. The symbols are: filled diamonds = detections, open diamonds with arrow = 3-sigma upper limits. The upper limits lie around the dotted line, above which the sources are brighter than 1% of the background. PG 1259+593 and PG 2112+059 were only observed with the less sensitive chopped mode. The diamond with plus represents the exceptional case of PG 0044+030, for which the 60 and 100 μm raster maps have been co-added.

from thermal dust emission as was previously shown for some quasars by Chini et al. (1989) and Hughes et al. (1993).

Even for the radio loud quasars PG 0044+030 and PG 1241+176 (with steep spectrum) and PG 1302-102 (with flat spectrum) the thermal bump is sharply rising above the synchrotron emission. PG 1302-102 was monitored at 1.3 mm over the last seven years, showing that the synchrotron activity was actually low at the time of the ISO observations in 1997. This means that the chance to detect a thermal bump was quite high. The confidence in the $60 - 100$ μm bump is strengthened by the upper limit at 170 μm. A similar case of a thermal bump above a relatively bright and flat (hence beamed) synchrotron spectrum was also found by ISO observations of the OVV quasar 3C279 (Haas et al. 1998a).

The IR SED of each quasar can be modelled by a superposition of several modified blackbodies (dust emissivity pro-

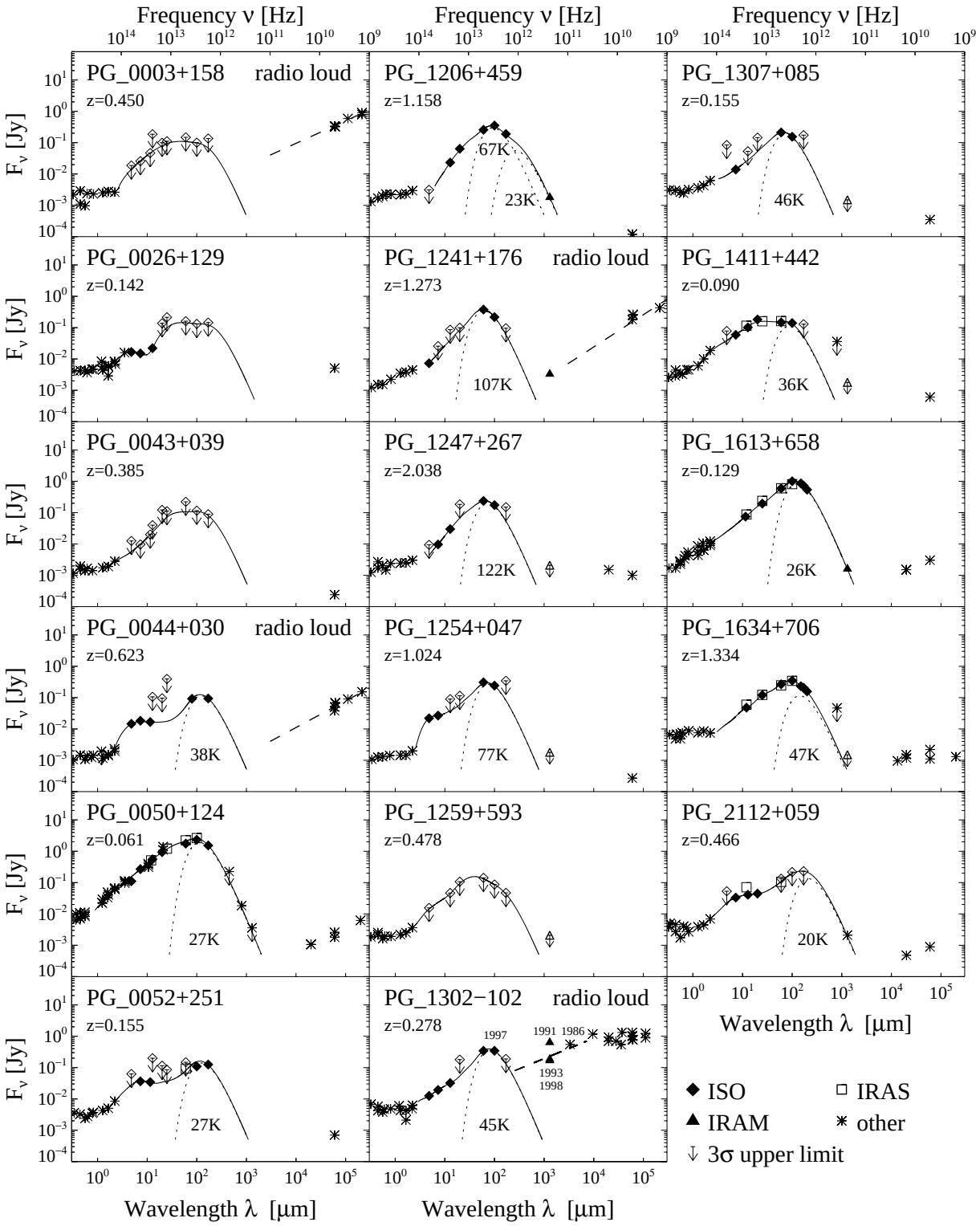

Fig. 2. Spectral energy distributions of our PG quasars. The wavelenght and frequency ranges are as observed and not corrected to the rest frame of the objects. Several modified blackbodies with emissivity proportional to λ^{-2} are eyeball fitted to the data (drawn lines) and only the coolest components are plotted individually (dotted lines). Where only upper limits are achieved (like in the case of PG 0003+158), the solid drawn lines indicate the range from which the luminosity limits in Table 2 are derived. The temperatures listed are corrected for redshift. The long-dashed lines indicate extrapolated synchrotron spectra. For the variable radio source PG 1302-102 different epochs of the data groups are indicated by the year. The literature data (asterisks) are in the optical from Neugebauer et al. (1987) and de Vaucouleurs et al. (1991), and in the radio regime from Steppe et al. (1988), Chini et al. (1989), Kellermann et al. (1989), Hughes et al. (1993), and Barvainis et al. (1996).

Table 1. Measured fluxes in mJy. Bold numbers are detections above the 3-sigma level, the errors are 10-30% of the quoted fluxes depending mainly on the source/sky brightness contrast as seen by the apertures used. The source/sky contrast (last column) is averaged for the wavelength range between 60 and 100 μm. The thin numbers represent 3-sigma upper limits. The * indicates those cases also detected with IRAS. The observing modes are: 1 = chopping with P1-C100, mapping with C200, 2 = mapping with all detectors P1-C200, 3 = chopping with P1-C100, sawtooth scan with C200, 4 = IRAM Bolometer at 1.3 mm. 'co-add' was applied to 60 and 100 μm maps resulting in a broad 80 μm band.

Object	Obs.	P1-Detector				P2-Detector		C100-Detector		C200-Detector			IRAM	source/sky
PG	Mode	4.8	7.3	11.5	12.8	20	25	60	100	150	170	200	1300	contrast
		μm	μm	μm	μm	μm	μm	μm	μm	μm	μm	μm	μm	
0003+158	2,3	<18	<27	<48	<186	<99	<111	<204	<231		<516			1
								<147	<99		<135			
0026+129	2,3	**17**	**15**		**22**	<138	<213	<228	<129		<315			1
								<162	<132		<144			
0043+039	2,3	<12	< 9	<21	<39	<123	<111	<300	<159		<126			1
								<222	<117		<90			
0044+030	2,3	**15**	**18**	**17**	<105	<96	<393	<303	<138					<1
	co-add							**92**			**94**			
0050+124	3	**110**	**269**		**554***	**936**	*	**1752***	**2339***		**1529**			>10
0052+251	2,3	<63	**36**	**34**	<198	<114	<87	<141	**163**		<198			1
								<147*	**109**		**125**			
1206+459	1,4	<3			**23**	**64**		**257**	**353**		**189**		**1.8**	3.5
1241+176	3,4	**7**	<27		<87	<99		**378**	**217**		<96		**3.3**	2.5
1247+267	3,4	<9	**10**		**30**	<183		**236**	**174**		<150		< 2.1	2
1254+047	3,4	**22**	**27**		<90	<114		**307**	**242**		<345		< 1.8	1.5
1259+593	1,4	<15			<45	<108		<141	<87		<48		< 2.1	1.5
1302-102	3,4	**13**	**19**		**32**	<180		**343**	**343**		<189		**635**	2
													168	
													185	
1307+085	3,4	<84	**14**		<54	<144		**212**	**155**		<174		< 1.5	1.5
1411+442	3,4	<78	**59**		**102***	**182**	*	**147***	**140**		<129		< 1.8	2
1613+658	2,4			**74**	*		**194***	**591***	**1002***	**858**	**730**	**539**	**1.6**	>10
1634+706	2,4			**48**	*		**120***	**267***	**349***	**230**	**206**	**158**	< 1.5	3.5
2112+059	3	<54	**33**		**41***	**45**		<135*	<216		<231			1

portional to λ^{-2}), indicating the presence of a wide variety of temperatures from hot (1000 K) to cool (30 K) dust in these objects. The temperature of the coolest dust component lies in the range between 30 and 120 K. Although our high redshift sample is small (5 sources at $1 < z < 2$), it seems remarkable that for all our sources the SED peaks close to 60 μm. As a consequence, the temperature of the coldest luminous dust component appears hotter the higher the redshift is (from 30 - 40 K at $z = 0$ to 90 - 120 K at $z = 2$). In one case (PG 1634+706) the IRAM 1.3 mm limit provides a constraint that the peak does not shift significantly towards the sub-millimetre range with redshift. For the other sources like PG 1206+459 or PG 1254+047 the 1.3 mm fluxes or upper limits still allow for an additional, relatively faint, cool dust component. For the radio loud source PG 1241+176, the 1.3 mm emission probably originates from the synchrotron radiation. Admittedly our sample is small, thus any dust temperature dependence on redshift is uncertain and the remarks are intended to point towards a possible trend. Further observations at sub-millimetre wavelenghts should enable us to clarify whether in quasars of earlier epoch or larger luminosity the coolest dust component really has a higher temperature, or whether the temperature trend appears just as an observational effect due to incomplete wavelength coverage of the current sparse data. Table 2 lists derived parameters like luminosities, dust temperatures and masses, supplemented by additional quantities used in the discussion.

5. Discussion

5.1. PG quasars are dusty

The spectra shown in Fig. 2 provide an impressive confirmation for the fact that the SED of an optically selected quasar contains a strong far infrared bump due to thermal emission by dust. The thermal infrared luminosities (Table 2) span three orders of magnitude, from luminous $10^{11}\,L_\odot$ to ultraluminous 10^{12}-$10^{13}\,L_\odot$, to hyperluminous $10^{14}\,L_\odot$ objects. For four out of five quasars for which we could establish only upper limits the resulting far infrared dust emission exceeds $10^{11}\,L_\odot$.

Our random sample provides a remarkably high mid and far infrared detection rate of 14/17. Thus we infer a low probability *p* that there exist dust-free naked quasars ($4/17 > p > 1/17$). The amount of dust lies in the order of $10^{7\pm1}\,M_\odot$ (Table 2) which is typical for dust rich spirals (cf. Haas et al. 1998b) as well as ULIRGs (cf. Klaas et al. 1997, + in preparation).

Table 2. Luminosities, dust temperatures and masses. The luminosity distance is determined as D_L = c / H_0 * (z + z^2 / 2), i.e. q_0 = 0, with H_0 = 75 km/sec/Mpc. The soft X-ray 0.1-2.4 keV luminosity L_X is derived from the ROSAT archive. Note that in the restframe of the quasar the X-ray window shifts according to z. The absolute blue luminosity L_B in the restframe of the quasar is derived from Véron-Cetty & Véron (1998). The infrared luminosities L_{IR} (3-1000 μm), L_{MIR} (3-40 μm) and L_{FIR} (40-1000 μm) are computed from the blackbody curves shown in Fig. 2. T_{dust} refers to the coldest dust component derived from the decomposition of the SED. The dust mass M_{dust} is estimated according to Hildebrand (1983). The SED shapes are binned into power law increase (1), MIR dominated (2), FIR dominated (3); for details see Sect. 5.2.2.

Object	z	D_L Mpc	L_X 10^9 $L_\odot$	L_B 10^9 $L_\odot$	L_{IR} 10^9 $L_\odot$	L_{MIR} 10^9 $L_\odot$	L_{FIR} 10^9 $L_\odot$	T_{dust} K	M_{dust} 10^5 $M_\odot$	L_{IR}/ L_B	L_{FIR}/ L_{MIR}	SED shape
0003+158	0.450	2203	812	765	< 4319	< 3790	< 529	29	< 982	<5.6	0.139	–
0026+129	0.142	608	108	160	< 329	249	< 80	17	<1992	<2.1	0.323	3
0043+039	0.385	1835	< 364	1009	< 1852	< 1426	< 426	27	< 1141	<1.8	0.299	–
0044+030	0.623	3266	282	1753	4247	3177	1070	38	1077	2.4	0.337	3
0050+124	0.061	251	35	92	803	575	228	27	983	8.7	0.396	1
0052+251	0.155	668	149	253	365	289	76	27	465	1.4	0.264	3
1206+459	1.158	7309	<3703	14582	45665	35996	9669	23	23901	3.1	0.269	2
1241+176	1.273	8327	<4563	14582	76877	71582	5295	107	88	5.3	0.074	2
1247+267	2.038	6448	5978	58052	197437	191048	6389	122	75	3.4	0.033	2
1254+047	1.024	6189	<2831	6979	36271	31579	4692	77	213	5.2	0.149	3
1259+593	0.478	2367	< 567	1599	< 5232	< 4681	< 551	33	< 367	<3.3	0.118	–
1302−102	0.278	1266	318	1106	1743	1094	649	45	281	1.6	0.593	1
1307+085	0.155	668	169	278	347	238	109	46	38	1.2	0.460	1
1411+442	0.090	376	3	121	269	239	30	36	27	2.2	0.125	2
1613+658	0.129	549	164	101	803	455	348	26	2113	8.0	0.765	1
1634+706	1.334	8889	1411	52944	88396	75895	12501	47	2004	1.7	0.165	1
2112+059	0.466	2297	15	1213	< 4539	3363	< 1176	20	< 18157	<3.7	0.350	2

Since the dust must have been produced by stars, this supports the hypothesis that the quasars are accompanied or proceeded by a starburst. Further arguments in favor of a starburst come from morphological observations (partly with the HST) where interactions with companions have been revealed, also for some of our sources like PG 0052+251 which is a spiral with a ring of HII regions (Dunlop et al. 1993; Bahcall et al. 1996, 1997), PG 1302-102 (Hutchings & Neff 1992; Disney et al. 1995), PG 1411+442 (Hutchings & McClure 1990), and PG 1613+658 (Disney 1998).

5.2. AGN and starburst components

What powers the enormous dust emission reaching up to about 10^{14} $L_\odot$? Though the AGN alone could provide sufficient heating energy (as shown below), the problem is to find a scenario in which the central luminosity can efficiently be transported to reradiate from cooler outer regions. Since the currently investigated models of pure AGN heating scenarios fail in a considerable number of cases, starbursts have been suggested as a second heating mechanism to be responsible for the FIR output (Rowan-Robinson 1995). Since only a limited number of AGN models has been thoroughly investigated, this conclusion is not compelling in the sense that a proper model for AGN heating might have yet escaped the theorist's imagination. Thus the AGN could still be the sole dominant heating source. In this section, first we consider the existing models and then look, how far our data can provide new insights.

5.2.1. Existing models

The broad range of dust temperatures challenges the models which try to describe the IR emission around AGNs. The PG quasars have blue colors and low E_{B-V} absorptions in the spectra of the broad line regions, but contain considerable amounts of dust (at least half of our sample has $M_{dust} > 10^7$ $M_\odot$). Therefore a non-spherical geometry like disk/torus might be required, with face-on or at least intermediate viewing angle.

A very thick and compact dust torus (Pier & Krolik 1992, 1993) can not provide the broad temperature range required. Also for a thick and extended torus/flared disk with an r^{-1} density profile (Granato & Danese 1994, hereafter GD; Granato et al. 1997, herafter GDF) as well as a tapered disk (Efstathiou & Rowan-Robinson 1995) the predicted IR spectra are too narrow: they fit only the MIR range and fall far below the observed high FIR luminosity. In order to achieve broad MIR and FIR spectra, GD and GDF had to reduce the central dust density and to shift dust into the outer regions. In their model they assumed a disk with a dust density profile which is *constant* with radius. But such a profile has no physical basis and is nowhere else found, thus we reject this artificial type of profile. Instead, more interesting is a clumpy torus as proposed by Krolik & Begelman (1988) with the advantage that the dust, when organised in clouds, can easier survive the extremely strong radiation field of the AGN. As mentioned by Efstathiou & Rowan-Robinson (1995) the clumpiness will tend to increase the dust temperature in the outer part of the torus, as the dust sees the inner and hotter part of the torus through the gaps between inner clumps.

Detailed results for a clumpy torus model, however, are not yet available. Though very promising, it has to be clarified, how far the required broad range of dust temperatures can be achieved with the AGN as the sole power source. In view of these (present) difficulties, enormous starbursts – or also cloud collisions (Harwit et al. 1987) – are required as the main heating power for the FIR emission.

Alternatively, a geometrically thin, warped disk in the host galaxy was proposed (Phinney 1989, Sanders et al. 1989), where due to the warp the concave "frontside" of the outer regions is directly illuminated by the central heating source. Though an elegant picture at first glance, a 3-dimensional radiative transfer calculation is still missing, and the warped disk as explanation for the full MIR and FIR continua could not yet be confirmed by other observations and several objections have been mentioned:

(1) Pier & Krolik (1992) argued that with a warped disk viewed face-on (as would be the case for the quasars) one should see the 9.7 μm silicate feature in emission, because the surface of the warped disk will always be hotter than the main body, but the expected silicate 9.7 μm feature has not been detected yet.

(2) Also, Rowan-Robinson (1995) argued that in at least some cases the FIR/UV-optical luminosity ratio is much too high to be explained with reprocessing by a dusty warped disk.

Note that Rowan-Robinson applied a conservative "violation criterion" requiring $L_{FIR} / L_{UV-opt} < \Omega$, with L_{UV-opt} being dereddened and $\Omega = 1$ being the violation threshold. Actually the violation threshold might be much lower: a warp with an inclination angle α° against the disk plane covers a fraction $\Omega = \alpha/180$ of the sphere, for example $\alpha = 18^\circ$ results in $\Omega = 0.1$, and $\alpha = 36^\circ$ results in $\Omega = 0.2$. The inclination angle might be at maximum 36°, otherwise the warp might become dynamically unstable and will be disrupted, leading rather to a distribution of clumpy clouds (which would no longer be described as warped disk model). Though a rough estimate, it shows that the violation threshold most likely lies at about $0.1 < \Omega < 0.2$.

Warps may exist in the disks of quasar host galaxies, but they might not be suited to explain the near- to far- IR spectra of quasars.

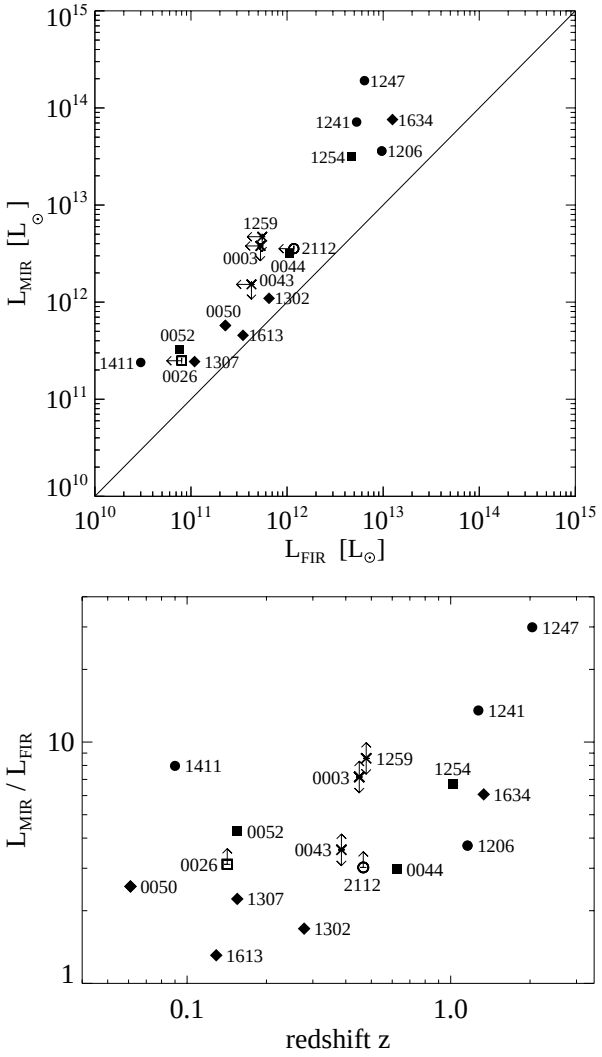

Fig. 3. Restframe mid- versus far-infrared luminosity of the PG quasars *(top)* and ratio L_{MIR}/L_{FIR} *(bottom)*. Different symbols for SED groups as in Table 2: (1) diamonds, (2) circles, (3) squares, (not classified) crosses.

5.2.2. The variety of the SED shapes

We now investigate our quasar data. The SEDs show a variety of shapes. In order to provide clues for the discussion of the heating mechanisms, we searched for distinct features in the SED shapes. As a result, we choose to bin the SEDs into three groups with the following features:

1) a power law rise from the NIR to the FIR, most prominent for the low redshift quasars PG 0050+124 and PG 1613+658, similar for the high redshift quasar PG 1634+706 (but with a flat intrinsic optical component).
2) a strong dominance of the MIR: the most prominent case is PG 1411+442, probably PG 2112+059, with NIR/MIR detection, but only upper limit in the FIR, also belongs to this group. Furthermore, the high redshift sources like PG 1247+267 (z>1) very likely belong to this group: Their FIR peaks intrinsically originate in the MIR and they could have an additional faint cool dust component (which then should be detectable in the submm range). The SEDs of group 2 typically seem to have also a power law like flux increase, but it last only from the NIR to the MIR (≈ 30 μm) and is therefore not as striking as for that of group 1.
3) two maxima: one in the NIR/MIR and a dominant one in the FIR, with a jump between 25 and 60 μm. PG 0044+030 and PG 0052+251 belong to this group.

Table 2 lists the classification of all 14 sources detected. Our current sample is obviously too small to decide, whether the proposed groups are clearly distinct or only represent an arbitrary binning of a continuous distribution of SED shapes. Nevertheless, the grouping of the SED shapes according to the three features as presented above seems to be a fruitful way to disentangle the heating mechanisms. The power law rise of the SEDs of group 1 indicates a well ordered dependence be-

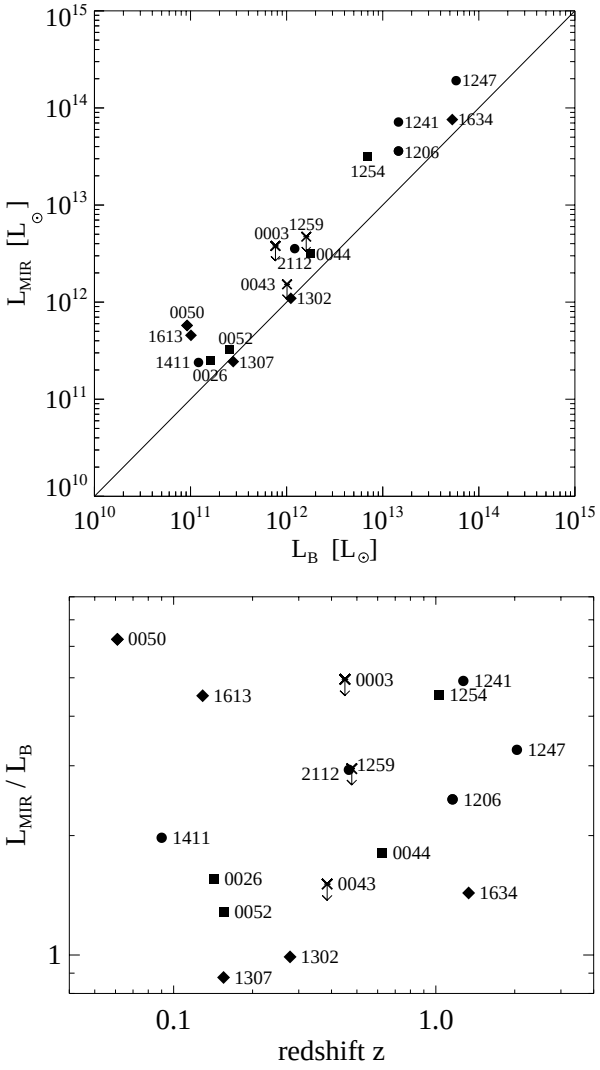

Fig. 4. Restframe mid-infrared versus blue luminosity of the PG quasars *(top)* and ratio L_{MIR}/L_B *(bottom)*. Different symbols for SED groups as in Table 2: (1) diamonds, (2) circles, (3) squares, (not classified) crosses.

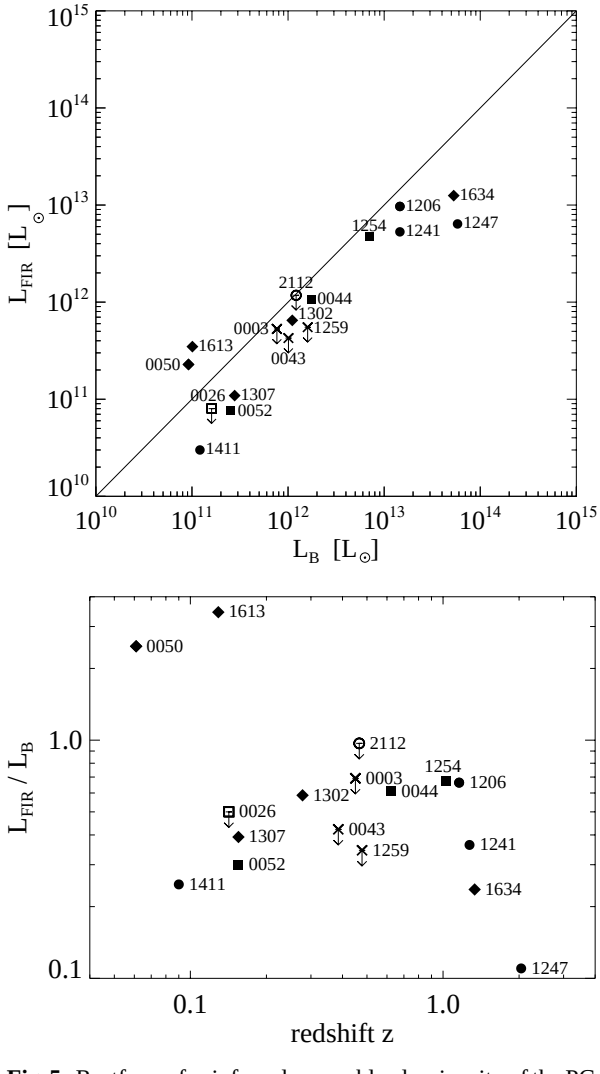

Fig. 5. Restframe far-infrared versus blue luminosity of the PG quasars *(top)* and ratio L_{FIR}/L_B *(bottom)*. Different symbols for SED groups as in Table 2: (1) diamonds, (2) circles, (3) squares, (not classified) crosses.

tween the different dust components. It suggests, in fact, heating by a central source with a temperature gradient from inside to outside. In the cooler regions starbursts could perhaps become significant. The SEDs of group 2 (having also some power law flux increase, but a high MIR contribution with respect to that in the FIR) can be understood in terms of a central heating without need for an additional starburst outside. On the other hand, the SEDs of group 3 (having a low MIR plateau with respect to that in the FIR) are more reminiscent of interacting starburst galaxies (cf. Klaas et al. 1997) and indicate either that a starburst is necessary, or that extinction plays a significant role, even in the MIR. However, there is no strong obscuration, since the L_{MIR}/L_B and L_{FIR}/L_B ratios are not exceptionally high as shown below.

The variety of SED shapes suggests that the MIR and the FIR emission originate from dust components, whose power sources are different or not directly coupled. Alternatively, the different SED shapes are caused by different scenarios. An attempt to describe all three SED groups by a single common model has to account for this diversity – a real challenge in addition to the broad range of dust temperatures.

5.2.3. The luminosity correlations

We consider now the restframe MIR and FIR luminosities of our whole sample. The MIR and FIR luminosities are correlated on a wide range, as shown in Fig. 3 (top) using the values from Table 2. This extragalactic MIR luminosity – FIR luminosity correlation, however, could be dominated by the large distance range involved, i.e. it could correlate mainly the distance with itself. Therefore Fig. 3 (bottom) shows the MIR/FIR luminosity ratio against redshift. This plot clearly demonstrates that there is a *broad scatter* of at least one order of magnitude, and also that there is no trend with SED shape. Nevertheless, on average the MIR luminosity is at least as high as that in the FIR. There

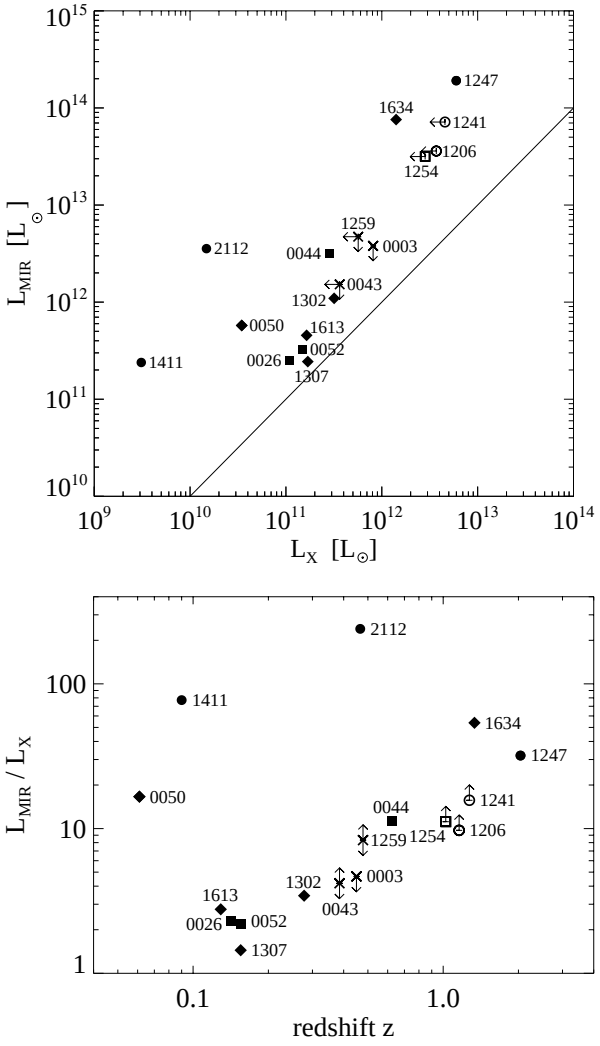

Fig. 6. Restframe mid-infrared versus soft-X-ray luminosity of the PG quasars *(top)* and ratio L_{MIR}/L_X *(bottom)*. Different symbols for SED groups as in Table 2: (1) diamonds, (2) circles, (3) squares, (not classified) crosses.

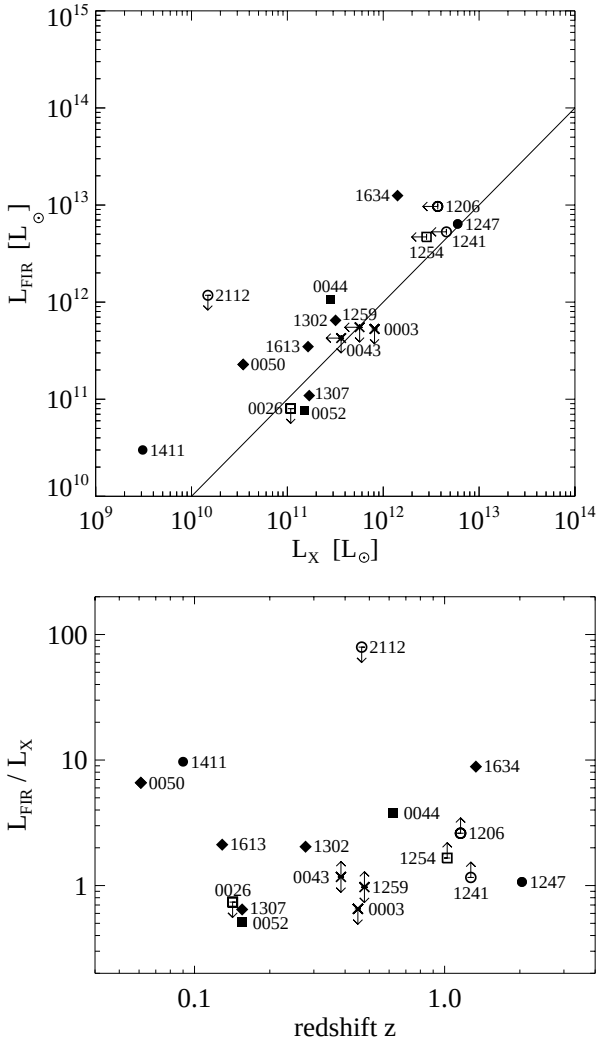

Fig. 7. Restframe far-infrared versus soft-X-ray luminosity of the PG quasars *(top)* and ratio L_{FIR}/L_X *(bottom)*. Different symbols for SED groups as in Table 2: (1) diamonds, (2) circles, (3) squares, (not classified) crosses.

is also a trend with redshift and/or bolometric luminosity: the more luminous sources have a higher MIR/FIR luminosity ratio. This color trend is not an artefact due to missing/unknown submm flux, since the maximum possible FIR luminosity can be well constraint by our IRAM 1.3 mm flux limits (see Fig. 2). In PG 1247+267 for example, an additional cool dust component hidden underneath the 1.3 mm flux limit would increase the FIR luminosity only by a maximum factor of two, hence the MIR/FIR trend with luminosity still remains.

Both the mid- and far-infrared luminosities are well correlated to the blue luminosity L_B (Figs. 4 and 5). There are no trends with SED shape. Remarkably both the L_{MIR}/L_B and L_{FIR}/L_B correlations are of similar quality. (The two L_{FIR}/L_B extremes PG 0050+124 and PG 1613+658 are discussed separately in Sect. 5.2.4 below.) The blue luminosity must originate from the central region, since it is extremely well correlated with the broad line Lyman$_\alpha$ luminosity (cf. Netzer 1990). Furthermore, a starburst in the dense central region is expected to show more reddening than observed, hence L_B does not come from a starburst. Since $L_{UV-opt} \approx 9 * L_B$, we get for all our quasars $L_{UV-opt} > L_{IR}$, hence the broad line region (BLR), in principle, can provide sufficient energy to account for the dust emission.

The blue/MIR/FIR luminosity correlations indicate a common heating source for the MIR and FIR dust components or a coupling between the different heating sources. In case of two heating sources – AGN *and* starburst – the correlations can qualitatively be interpreted as proposed by Rowan-Robinson (1995): the more massive and powerful the starburst, the more likely it is for the matter to have an unstable angular momentum and drop into the black hole. The AGN then strongly heats the central dust component. There are of course individual irregularities, reflected by the different SED shapes and the scatter shown in Fig. 3 bottom, which could be caused by different extinction/aspect angles or evolutionary states.

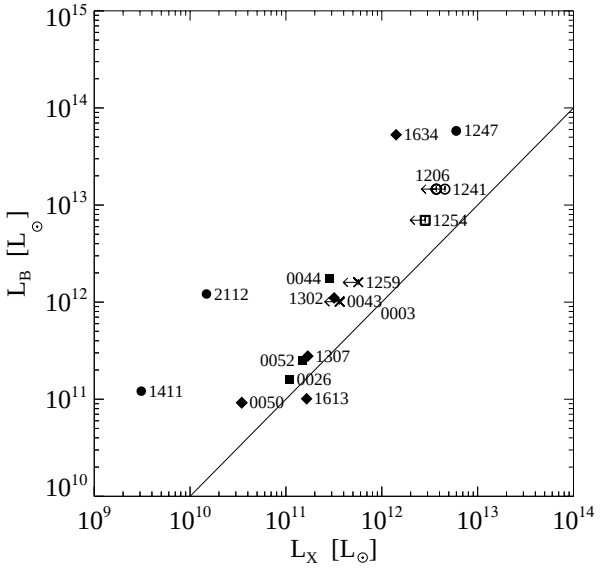

Fig. 8. Restframe blue luminosity versus soft-X-ray luminosity of the PG quasars. Different symbols for SED groups as in Table 2: (1) diamonds, (2) circles, (3) squares, (not classified) crosses.

If the FIR emission is mainly caused by starburst, then supernova remnants (SNRs) will play a significant role. Since SNRs are also powerful X-ray emitters, we looked for a correlation between the MIR and FIR luminosities and the soft X-ray luminosities we derived from the ROSAT archive. Such correlations are present, but weak (Figs. 6 and 7). The soft X-rays (0.1-2.4 keV) are believed to originate from the AGN (the accretion disk or the corona or a jet) as well as from SNRs. If they come primarily from SNRs, then the L_{FIR}/L_X correlation should be better than the L_{MIR}/L_X one. But within the scatter of the distributions this is not observed (and in addition some sources are X-ray variables), thus the soft X-rays cannot be used to support the starburst hypothesis. Furthermore, the L_{FIR}/L_X ratios of our quasars lie between 0.5 and 10, and hence are considerably lower than typical values of about 10-100 found for SNRs in the Milky Way (G. Hasinger, private communication; see also Dwek et al. 1987). Therefore the soft X-rays might originate from the AGN, i.e. its accretion disk or its corona. (We do not consider the jet possibility since most of our sources are radio quiet.) Note the trend that the MIR dominated SED group 2 shows the highest L_{MIR}/L_X and L_B/L_X ratios. Interestingly, the scatter in the L_X to L_B correlation (Fig. 8) indicates a variety in soft X-ray generation and absorption of the central region. An interpretation could be that, if the black hole is fueled at about maximum rate (Eddington limit), then a lot of matter is centrally located which also could act as an X-ray absorber.

5.2.4. The remaining puzzle

So far we arrived at a consistent picture in which the quasars with strong MIR bump (SED group 2) can be well understood in terms of a pure AGN heated dust torus with no evidence for starbursts. And those quasars with strong FIR bump (SED group 3) look as though they definitely require a starburst. Nevertheless the question remains, why in these sources the starburst luminosity is of similar order as the AGN luminosity. Interestingly, other correlations between nucleus and extended regions have been found, too: (1) In the near infrared, the luminosity of the central unresolved point source increases with that of the host galaxy (McLeod & Rieke 1994a, 1994b), and (2) the mass of the black hole as derived from H_β lines shows a clear trend with the optical luminosity of the bulge of the host galaxy (Laor 1998).

Problematic objects in the picture of two heating sources are those with the long lasting power law flux increase from the NIR to the FIR (SED group 1). The two sources PG 0050+124 and PG 1613+658 lie clearly above the main population in the L_{FIR}/L_B diagram (Fig. 5), while in the L_{MIR}/L_B diagram (Fig. 4) they lie closer to the mean, indicating for these two sources either that in case of pure AGN heating a special scenario is required or that a strong starburst contributes significantly to the FIR luminosity. In the latter case the SED of group 1 could be understood as suited combination of SED group 2 and 3. Though possible, it seems somewhat unlikely that two relatively independent heating mechanisms produce such an extremely smooth flux increase from the NIR to the FIR. This suggests that the SED group 1 has to be fully explained with the AGN as the dominant power source and that the proper geometry or scenario has to be searched for and thoroughly investigated. The most promising scenario seems to be the clumpy torus model. (The warped disk model might be discarded for PG 0050+124 and PG 1613+658 which have $L_{FIR}\,/\,L_{UV-opt} \approx 0.3 > \Omega$ (see Sect. 5.2.1)).

Interestingly, the SEDs of some sources (these are just PG 0050+124 and PG 1613+658 with SED group 1) fall off extremely steep beyond their maximum flux at about 100 μm. It is not yet clear (Fig. 2), how the fall-off is for the other sources or SED groups, and whether a difference in the fall-off behaviour can be established. The steep spectral fall-off means that on the "cool side" there is no steady layering of several considerable colder dust components which are possibly distributed more outside and diffusely within the host galaxy. Any luminosity contribution from such a layering is negligible. This suggests that among the luminous ones there exists a well defined coolest dust component, which probably also has a well defined spatial extent. The coolest dust component could also be the consequence of a high, but homogenous diffuse "interstellar" radiation field distributed throughout the host galaxy.

5.3. Relation to ULIRGs

All our detected quasars have high IR luminosities, and also the few cases with upper limits allow for considerable IR luminosity. Remarkably all of our detections also have warm MIR/FIR colors, $F_{25\mu m}/F_{60\mu m} > 0.2$, ranging from 0.3 to 1.25 with a median about 0.5, whereby we corrected for the redshift effects. Therefore our result just provides the sought after evidence for the reverse direction of the link between warm ULIRGs and quasars proposed by Sanders et al.(1988b): out of their bright ULIRG sample with warm MIR/FIR colors all 12 of 12 sources

showed optical signatures of quasars. Formally expressed we have now:

(a) warm U-LIRG $\Rightarrow$ optical quasar (Sanders et al.)

(b) warm (U)LIRG $\Leftarrow$ optical quasar (this work).

Since ULIRGs with warm MIR/FIR colors show optical signatures of a quasar, the central region as well as the inner part of the torus is neither heavily obscured in the optical nor in the MIR. Thus the warm ULIRGs are seen face-on or at intermediate viewing angles, but not perfectly edge-on.

What are the edge-on counterparts of PG quasars? Among ULIRGs, particularly those with warm MIR/FIR colors have been proposed to be dust-enshrouded quasars (Sanders et al. 1988a), but several objections have been mentioned. Therefore we discuss the two most commonly quoted objections and argue that even a *cool* ULIRG could be a dust-enshrouded quasar:

(1) The luminosity function of ULIRGs indicates too a high volume density compared with that of quasars (Rowan-Robinson 1995). Since not every ULIRG needs to be an edge-on PG quasar, the discrepancy between the luminosity function of ULIRGs and the (faint) end of PG quasars can be explained. Also, the fainter quasars could be still evolving and more dusty, hence fainter and more reddened and therefore optically not yet identified as quasars. Recent investigations of the quasar and ULIRG luminosity functions (Krishna & Biermann 1998) which include two new quasar surveys show that quasars are at least as numerous in the local universe as ULIRGs. Thus the argument using the luminosity function is discredited.

(2) MIR spectroscopy with ISO (Genzel et al. 1998) shows that most of the ULIRGs exhibit strong PAH features characteristic for starbursts and do not show bright lines of sufficiently high exitation characteristic for a dominating AGN. On the other hand, in quasars and some warm ULIRGs high exitation lines were detected, but only upper limits for PAH features. The interpretation of these observational differences in favor of starburst or AGN rely on the geometry assumed and on whether the spectral features/lines are all measured at a comparable contrast (i.e. signal/noise ratio) above the continuum. But these assumptions might be violated in case of a non-spherical geometry in which the PAH features arise from outer regions and the high exitation lines from nuclear regions which are outshining or extinguished depending on aspect angle. Remarkably, recent ISO spectroscopy on Seyfert galaxies (Schulz et al. 1998) indicates that – compared to Seyfert 1 galaxies – in Seyfert 2 galaxies the 6 - 12 μm continuum, i.e. the inner torus emission, is severely suppressed, probably by the outer torus parts. This suggests that also in edge-on PG quasars (the bright end of Seyfert 2s) the torus (or disk) might be opaque to its own MIR radiation and the nuclear high excitaton lines. Hence, the validity of the objection via MIR spectroscopy is reduced.

From our data the dust mass and the opacity can be estimated relatively free from any screen bias, since the FIR radiation might be optically thin. Distributing a dust mass of 10^8 $M_\odot$ (e.g. for PG 0050+124, see Table 2) homogeneously within a slab of 100 pc height and 1000 pc radius yields dust column density of about 30 $M_\odot$ pc^{-2} face-on and 300 $M_\odot$ pc^{-2} edge-on (Fig. 9).

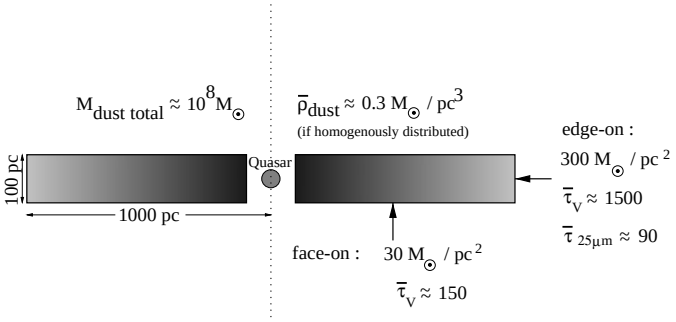

Fig. 9. Schematic of a dusty slab illustrating the opacity when seen face-on and edge-on.

Adopting a common conversion of 0.1 $M_\odot$ pc^{-2} to $\tau_V \approx 0.5$ yields an opacity $\tau_V \approx 150$ for face-on and $\tau_V \approx 1500$ for edge-on view. Using $A_{25\mu m}$ / $A_V \approx 0.063$ (see Mathis et al. 1983) yields an edge-on mid-infrared optical depth of $\tau_{25\mu m} \approx 90 \gg 1$. Though a rough estimate, it also yields for reasonably larger slab heights and smaller radii as well as an r^{-1} dust density profile, that the edge-on viewed disk/torus is opaque to its own central MIR radiation. And this might also hold for a *clumpy* torus.

Thus we conclude that an edge-on PG quasar will appear to us like an ULIRG with an SED modulated by extinction, hence having even cool MIR/FIR colors ($F_{25\mu m}/F_{60\mu m} < 0.2$). However, not every ULIRG SED shows signatures of such an extinction: e.g. NGC 6240 has a clear MIR plateau, while Arp 220 is more reddened (Klaas et al. 1997). Interestingly, the cool ULIRG IRAS 15250+3609 shows a strongly reddened power law MIR to FIR SED (Klaas et al. 1998a) and a Seyfert 2 type spectrum (Sanders et al. 1988a), suggesting an edge-on quasar. Nevertheless, not every ULIRG needs to be a quasar or evolve into one, but the IR SEDs can help to find candidates. Since the extinction and reddening in the optical, UV and even the soft X-ray range is extremely high for an edge-on quasar, such a source would never be identified as a quasar via common selection criteria. In particular, the blue luminosity would be severely underestimated (also in case of a luminous extended host galaxy), and probably the (soft) X-ray power, too. However, a (polarised) Seyfert 2 type spectrum might remain recognisable.

6. Summary

Infrared to millimeter spectral energy distributions (SEDs) have been obtained for a random sample of 17 Palomar Green quasars with ISO between 4.8 and 200 μm and, for ten of these sources, with IRAM at 1.3 mm. Eight sources were detected for the first time in the far infrared. The SEDs generally peak around 60 μm and decline onward of 100 μm down to low fluxes at 1.3 mm, providing strong evidence for thermal dust emission. The dust mass lies in the order of $10^{7\pm1}$ $M_\odot$. We find only a low probability ($p < 4/17$) for the existence of dust-free, naked quasars supporting the hypothesis that every quasar is surrounded by dust and probably accompanied by a starburst.

The spectra show a variety of shapes which we have tentativly binned into three groups characterised by the following features: (1) a power law like flux increase, (2) a MIR bump and (3) a step like increase between relatively constant MIR and FIR flux plateaux. Irrespective of the SED shapes, the $3-40\,\mu$m MIR luminosity is correlated with that integrated over the $40-1000\,\mu$m FIR range, and both correlate well with the blue luminosity, and somewhat also with the soft X-ray luminosity. While in all sources the MIR emission might be powered by the AGN, those quasars of group 3 having a high FIR/MIR ratio require an enormous starburst. This confirms previous findings by Rowan-Robinson (1995) that the relation between AGN and starburst may be understood as follows: a turbulent environment which favors a strong starburst also likely disturbs the angular momentum of gas clouds which are then channeled inwards and feed the AGN. However, in the group 1 quasars with power law flux increase from the NIR to the FIR the dependence between the dust components at different temperatures appears so smooth that independent heating mechanisms seem unlikely. Thus in these quasars the dust might be heated primarily by the AGN. Since the current models cannot fit the power law spectra up to the FIR, the observations suggest an elaboration of the clumpy torus model to be the most promising, where the central radiation can travel though the gaps between the clumps farther out in order to provide sufficient FIR emission.

Our optically selected quasars posses thermal infrared luminosities over three orders of magnitude: from luminous $10^{11}\,L_\odot$ to hyperluminous $10^{14}\,L_\odot$. They exhibit warm MIR/FIR colors ($F_{25\mu m}/F_{60\mu m} > 0.2$) providing evidence that the converse of a previous relation (Sanders et al. 1988b) between warm ultraluminous infrared galaxies (ULIRGs) and quasars also holds. Since PG quasars have blue optical colors and low extinction, but are also dust rich, a non-spherical disk/torus geometry has to be involved which is seen face-on or at intermediate angles. Even in the MIR a high edge-on optical depth is derived from our dust masses. Then any candidates for edge-on PG quasars will appear to us like ULIRGs with even cool MIR/FIR colors ($F_{25\mu m}/F_{60\mu m} < 0.2$). But not every ULIRG needs to be a dust-enshrouded quasar.

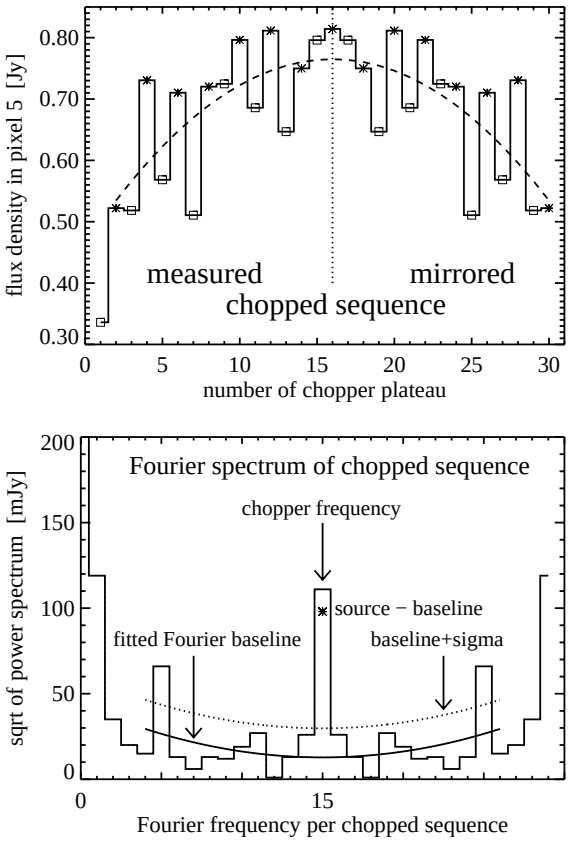

Fig. A.1. Example of a chopped sequence (*top*) and its Fourier spectrum (*bottom*). Before Fourier transformation, the measured sequence was mirrored (around the vertical dotted line). This is important in case of a long term drift which is indicated by the dashed line. This removes the jump and guarantees a continuous periodic sequence and thus reduces sidelobe noise in the power spectrum. In Fourier space the source signal shows up at the chopper frequency, while the noise of the chopped sequence forms some kind of baseline distributed over all frequencies; the effect of the long term drift shows up at the low frequencies in the baseline. Since the chopper frequency is the highest frequency occuring in the Fourier spectrum, in this plot the Fourier spectrum is also mirrored around the chopper frequency for the purpose of a better visual impression of the source signal sitting above the baseline and its scatter. The final source signal (asterisk) is derived after subtraction of a suitable baseline fitted by a parabola, and sigma is determined from the scatter of the baseline around this parabola. Note that sigma in the Fourier space is considerably smaller than in the chopped sequence.

Appendix A: advanced ISOPHOT data reduction

This paper deals with faint sources near the detection limit and the results depend critically on a solid data reduction. Therefore for the critical reader the main tools are described here in detail. Also, a look at the figures gives a valuable feeling for the data quality.

A.1. Fourier analysis of chopped data

For the chopped measurements we applied a Fourier analysis as illustrated in Fig. A1. It is quite robust against single outlier chopper plateau signals and the effect of long term detector drift. Its main advantage is a consistent noise estimate which also accounts for the number of chopper plateaux: Various measurement series (taken from the ISO archive) with the same total on-source integration time, but with one series having *many short* chopper plateaux and another having *few long* chopper plateaux, were compared. A standard PIA data reduction yielded different sigma values (those series with short chopper plateaux appeared noisier, since the number of chopper plateaux was not accounted for), but the Fourier analysis gave similar sigma values for all series. Empirically we found that sigma $_{\rm Fourier}$ is proportional to sigma $_{\rm PIA} * n^{-0.1}$ with n = number of chopper plateaux. Thus our sigma $_{\rm Fourier}$ still has the meaning of the *rms* and is not the *error of the mean* which would be proportional to $n^{-0.5}$, i.e. much smaller.

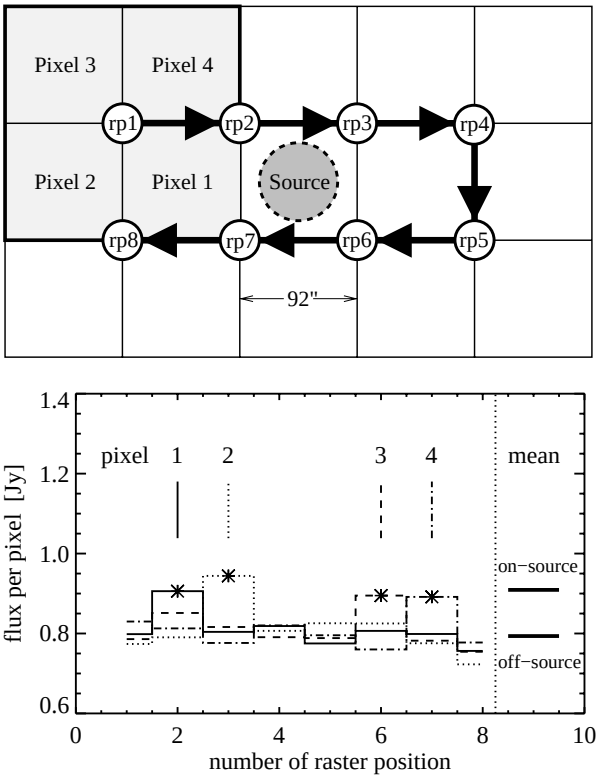

Fig. A.2. Scheme of a raster map with the C200 detector and its analysis.

top: Small 4×2 raster map with the 2×2 pixel C200 detector array (shadowed), resulting in a map with a size of 5×3 pixels. During the raster map each detector pixel is centered on the source exactly once.

bottom: Signal time series for each pixel shown by a different linestyle. The asterisks and vertical lines indicate those raster points on which the pixel *j* is expected to hit the source. The mean on- and off-source signals are also shown on the right hand side.

A.2. Time series analysis of raster maps

For the small raster maps we did not extract the source flux from the final maps. Instead, we analysed the signal time series while each detector pixel crossed the source. This is illustrated for a relatively bright source observed with the C200 detector (Fig. A2) and for our faintest one with the C100 detector (Fig. A3). This technique allows immediate recognition of bad or outlying signals. Furthermore, a long term detector drift could increase the scatter in the background values of a map, while for the time series of each detector pixel the background can be estimated more accurately from the raster positions located immediately before and after the source was hit. (Since the Airy disk is larger than the size of one pixel, in principle some source flux is detected by the pixels on the adjacent raster positions, i.e. just those from which the background was estimated. But – as we obtained from the beam profiles – this offset is clearly less than 5% of the source flux, hence negligible within the other errors.) The final source signal is then derived from the mean of the signals for the *j* detector pixels, whereby outliers are clipped. Finally, assuming an unresolved point

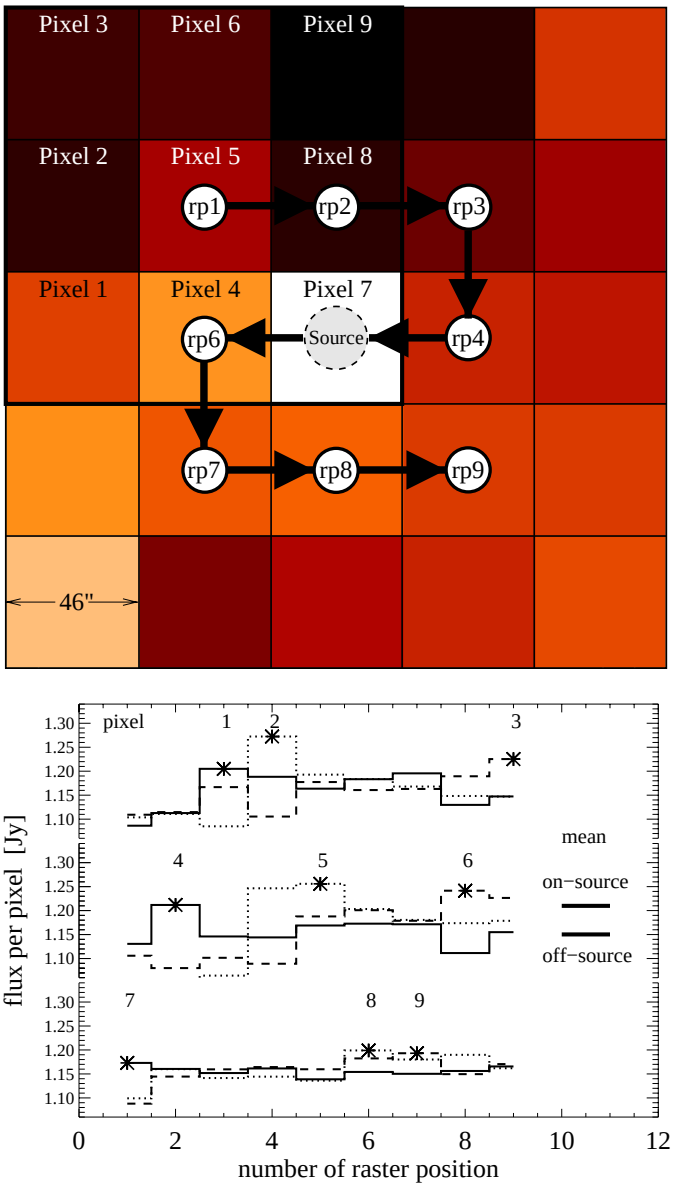

Fig. A.3. Raster map with the C100 detector and its analysis. The example shown is the faintest one of our quasar detections, where we co-added the 60 and 100 μm time series (PG 0044+030).

top: Grey level map with overlay of the raster scheme. The small 3×3 raster map with the 3×3 pixel C100 detector array (shadowed) results in a map with a size of 5×5 pixels. During the raster map each detector pixel is centered on the source exactly once. The grey levels from black to white give the different flux intensities with the highest flux at the source position.

bottom: The signal time series of a 3×3 raster map with the 3×3 pixels C100 array, each pixel in a column having a different linestyle. The asterisks indicate those raster points on which the pixel *j* is expected to hit the source. For all 9 detector pixels a positive source signal is derived above the signals from the neighbouring background raster points. Nevertheless the noise is quite high, mainly caused by the long term drift (e.g. pixel 7 hits the source at the first raster point and yields a too small source flux) and residuals from glitches (e.g. the on-source position of pixel 2 or the lefthand background position of pixel 5). The mean of all on- and off-source signals are also shown on the right hand side.

source the fluxes are corrected for losses due to the aperture size.

Acknowledgements. We wish to thank the anonymous referee for constructive suggestions. It is a pleasure to thank Marcus Albrecht for supporting us in the IRAM data reduction. The development and operation of ISOPHOT and the data reduction are supported by MPIA and funds from Deutsches Zentrum für Luft- und Raumfahrt (DLR, formerly DARA). For literature and photometry search NED and SIMBAD were used.

References

Bahcall J.N., Kirhakos S., Schneider D.P., 1996, ApJ 457, 557
Bahcall J.N., Kirhakos S., Saxe D.H., Schneider D.P., 1997, ApJ 479, 642
Barvainis R., 1990, ApJ 353, 419
Barvainis R., Lonsdale C., Antonucci R., 1996, AJ 111, 1431
Chini R., Kreysa E., Biermann P.L., 1989, A&A 219, 87
de Vaucouleurs G., de Vaucouleurs A., Corwin jr. H.G., et al., 1991, Third reference catalog of bright galaxies. Version 3.9, Springer-Verlag, Berlin
Disney M.J., 1998, Scientific American 278, 52
Disney M.J., Boyce P.J., Blades J.C., et al., 1995, Nat 376, L150
Dunlop J.S., Taylor G.L., Hughes D.H., Robson E.I., 1993, MNRAS 264, 455
Dwek E., Petre R., Szymkowiak A., Rice W.L., 1987 ApJ 320, L27
Efstathiou A., Rowan-Robinson M., 1995, MNRAS 273, 649
Genzel R., Lutz D., Sturm E., et al., 1998, ApJ 498, 579
Granato G.L., Danese L., 1994, MNRAS 268, 235 (GD)
Granato G.L., Danese L., Franceschini A., 1997, ApJ 486, 147 (GDF)
Haas M., Chini R., Meisenheimer K., et al., 1998a, ApJ 503, L109
Haas M., Lemke D., Stickel M., et al., 1998b, A&A 338, L33
Harwit M., Houck J.R., Soifer B.T., Palumbo G.G.C., 1987, ApJ 315, 28
Herbstmeier U., Abraham P., Lemke D., et al., 1998, A&A 332, 739
Hildebrand R.H., 1983, QJRAS 24, 267
Hooper E.J., Wilkes B.J., McLeod K., et al., 1999, In: Cox P., Kessler M. (eds.) The universe as seen by ISO. ESA publications, Noordwijk, p. 893
Hughes D.H., Robson E.I., Dunlop J.S., Gear W.K., 1993, MNRAS 263, 607
Hutchings J.B., McClure R.D., 1990, PASP 102, 48
Hutchings J.B., Neff S.G., 1992, AJ 104, 1
Kellermann K.I. Sramek R., Schmidt M., et al., 1989, AJ 98, 1195
Kessler M.F., Steinz J.A., Anderegg M.E., et al., 1996, A&A 315, L27
Klaas U., Radovich M., 1998, Report on the ISOPHOT scientific validation for OLP V7.0, ISO Explanatory Library Rep. SAI/98-049/rp, ESA publications, Villafranca
Klaas U., Krüger H., Heinrichsen I., et al., 1994, ISOPHOT Observers Manual. Version 3.1, ESA publications, Villafranca
Klaas U., Haas M., Heinrichsen I., Schulz B., 1997, A&A 325, L21
Klaas U., Haas M., Schulz B., 1998a, In: Cox P., Kessler M. (eds.) The universe as seen by ISO. ESA publications, Noordwijk, p. 901
Klaas U., Laureijs R., Radovich M., Schulz B., 1998b, ISOPHOT calibration accuracies. ISO Explanatory Library Doc. SAI/98-092/rp, ESA publications, Villafranca
Kreysa E., Gemünd H.-P., Gromke J., et al. 1998, SPIE 3357, 319
Krishna G., Biermann P.L., 1998, A&A 330, L37
Krolik J.H., Begelman M.C., 1988, ApJ 329, 702
Laor A., 1998, ApJ 505, L83
Laureijs R., Klaas U., 1999, ISOPHOT Error Budgets V1.0, ISO Explanatory Library Doc. SAI/98-091/dc, ESA publications
Laureijs R., Klaas U., Richards P.J., Schulz B., 1998, ISOPHOT Data Users Manual, V4.0, ISO Explanatory Library Doc. SAI/95-220/dc, ESA publications
Lemke D., Klaas U., Abolins, et al., 1996, A&A 315, L64
Mathis J.S., Mezger P.G., Panagia N., 1983, A&A 128, 212
McLeod K.K, Rieke G.H., 1994a, ApJ 420, 58
McLeod K.K, Rieke G.H., 1994b, ApJ 431, 137
Netzer H., 1990, In: Blandford R.D., Netzer H., Woltjer L. (eds.) Active Galactic Nuclei. Springer-Verlag Lecture Notes, p. 135
Neugebauer G., Miley G.K., Soifer B.T., Clegg P.E., 1986, ApJ 308, 815
Neugebauer G., Green R.F., Matthews K., et al., 1987 ApJS 63, 615
Phinney E.S. 1989, In: Meyer F., Duschl W., Frank J., et al. (eds.) Theory of Accretion Disks. Kluwer Academic Publishers, p. 457
Pier E.A., Krolik J.H., 1992, ApJ 401, 99
Pier E.A., Krolik J.H., 1993, ApJ 418, 673
Rowan-Robinson M., 1995, MNRAS 272, 737
Sanders D.B., Soifer B.T., Elias J.H., et al., 1988a, ApJ 325, 74
Sanders D.B., Soifer B.T., Elias J.H., et al., 1988b, ApJ 328, L35
Sanders D.B., Phinney E.S., Neugebauer G., et al., 1989, ApJ 347, 29
Schmidt M., Green R.F., 1983, ApJ 269, 352
Schulz B., Clavel J., Altieri B., et al. 1998, In: Cox P., Kessler M. (eds.) The universe as seen by ISO. ESA publications, Noordwijk, p. 965
Steppe H., Salter C.J., Chini R., et al., 1988, A&AS 75, 317
Véron-Cetty M.P., Véron P., 1998, ESO Scientific Report: A Catalogue of Quasars and Active Nuclei (8th Edition). ESO, Garching
Wilkes B.J., Hooper E.J., Mc Leod K.K., et al.. 1999, In: Cox P., Kessler M. (eds.) The universe as seen by ISO. ESA publications, Noordwijk, p. 845